Materials and Design 172 (2019) 107758

Contents lists available at ScienceDirect

Materials and Design

journal homepage: www.elsevier.com/locate/matdes

Design, microstructure and mechanical characterization of Ti6Al4V reinforcing elements for cement composites with fractal architecture

Ilenia Farina [a], Russell Goodall [b], Everth Hernández-Nava [b], Andrea di Filippo [c], Francesco Colangelo [a,*], Fernando Fraternali [c]

[a] Department of Engineering, University of Naples "Parthenope", Naples, Italy
[b] Department of Materials Science & Engineering, University of Sheffield, UK
[c] Department of Civil Engineering, University of Salerno, Italy

HIGHLIGHTS

- A general procedure for the design of reinforcing elements with fractal architecture is presented.
- Physical models of Koch fibers and meshes are additively manufactured through electron beam melting.
- The accuracy of the reproduction of fractal geometries through additive manufacturing is investigated.
- The mix design and the mechanical characterization of a cement mortar to be reinforced with Koch fibers are given.
- Bending tests on mortar specimens reinforced with Koch fibers show marked matrix-rebar interlocking effects.

GRAPHICAL ABSTRACT

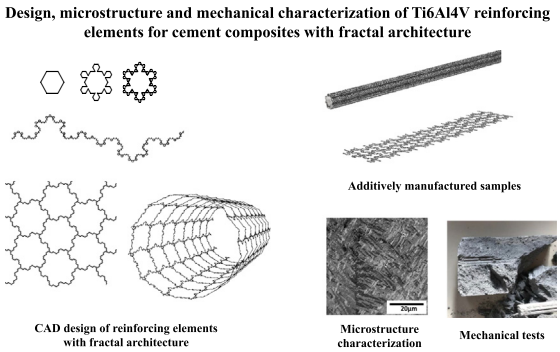

ARTICLE INFO

Article history:
Received 11 February 2019
Received in revised form 22 March 2019
Accepted 22 March 2019
Available online 29 March 2019

Keywords:
Fractal geometry
Koch curve
Fractal interlocking
Additive manufacturing
Titanium alloy

ABSTRACT

This paper presents a study on the design, and microstructural and mechanical characterization of additively manufactured reinforcing elements for composite materials exhibiting fractal geometry, with a focus on the flexural reinforcement of cement-matrix composites. The examined elements are manufactured via an additive process, electron beam melting, from the Ti6Al4V titanium alloy, using a Koch curve construction ruled by three complexity parameters. Koch fibers and meshes are designed, additively manufactured and experimentally tested, through the use of the proposed fractal design procedure. Laser scanning tests illustrate the correspondence between the CAD objects and the additively manufactured samples. The experimental characterization of the surface properties of the Koch fibers is conducted through optical microscopy and contact angle tests, while their mechanical performance is analyzed through Vickers hardness and bending tests on a fiber-reinforced reinforced mortar. The given mechanical tests highlight that reinforcing fibers with fractal architecture significantly enhance the first crack strength and the residual loading capacity of cement mortar specimens subject to three-point bending tests. This is due to the relevant interlocking mechanisms acting at the interface between the matrix and the ribs of such reinforcing elements, which delay the macroscopic cracking of the mortar.

* Corresponding author.
E-mail addresses: ilenia.farina@uniparthenope.it (I. Farina), r.goodall@sheffield.ac.uk (R. Goodall), e.hernandeznava@sheffield.ac.uk (E. Hernández-Nava), andrea.difilippo@unisa.it (A. di Filippo), francesco.colangelo@uniparthenope.it (F. Colangelo), f.fraternali@unisa.it (F. Fraternali).

https://doi.org/10.1016/j.matdes.2019.107758

1. Introduction

The development of novel materials fabrication processes is attracting growing interest from scientists and engineers towards architected materials and structures [1]. Recent advances in materials science have made increasingly possible the design of hierarchical elements exhibiting advanced mechanical properties at different scales [2–10]. Particularly interesting are the effects created by a hierarchical design of multiscale fibers coated with carbon nanotubes and different nanofibers, which have been proven to markedly enhance the interlaminar shear strength of multiscale composites [11–15]. Significant improvements in mechanical properties have also been observed in the presence of nanoscale coating on microlattices [16], nested hierarchical wrinkling patterns on polymeric surfaces created through plasma treatment [17], and a variety of other different surface treatments [18–19].

It is known that most natural materials exhibit hierarchical organization of matter and fractal geometries, which provide increased surface area for the same volume of material [20]. Fractal geometry indeed permits the design of hierarchical patterns through self-similar subdivisions of basic shapes such as squares or triangles. This subdivision process can be repeated an infinite number of times, obtaining increasingly complex structures that exhibit fractal dimensions much greater than their topological dimensions [20–23]. Fractals have been employed in a large variety of fields, including biology, economy, bio-architecture, electrical engineering, and in a number of different technologies (refer, e.g., to [24] and references therein). Particularly interesting is the fractal modeling of fractures and sutures in engineering and biological systems, as well as the fractal description of the topological interlocking occurring in architectured materials that are obtained by joining similar or dissimilar materials through interfaces with complex geometry [24–26]. The application of fractal concepts for the design of multiscale reinforcing fibers of composite materials, however, has not been significantly explored at the current date, with the exception of a few, limited scope examples, concerned, e.g., with tissue fiber scaffolds for biological applications [27].

Generally, the design of new objects relies on two main features, the chemical composition of the material and the morphological structure of the object. While the chemical composition is an intrinsic property of materials, their morphology and surface roughness can be artificially modified through suitable treatments that induce hierarchical architectures [19,20]. Surface treatments and coatings have been employed to design hierarchical structures based on carbon nanotubes [21,22] exhibiting an increase in fracture toughness; nanofibers featuring an increased redistribution of the load and thus improving the mechanical performance of each hierarchical system [1,24]; and films showing improved bonding and fracture toughness [25–27].

Additive manufacturing (AM) is currently the most common technique for fabricating architectured materials exhibiting advanced functionalities not found in conventional materials at different scales [28–29]. A large variety of additive manufacturing processes are available from the nanometre to the centimetre scale, such as stereolithography, laser sintering polyjet, x-ray lithography, electron beam melting and atomic layer deposition, to name just a few examples (while in some instances these processes are referred to as *3D printing*, here we use the term *Additive Manufacture*, *AM*). AM has made possible the fabrication of fractal shapes directly from computer-aided design (CAD) data, using metallic (steel, aluminum, titanium, etc.), polymeric (polypropylene, polyethylene terephthalate, etc.), natural (flax, jute, kenaf, etc.), recycled (plastic, glass, metals, rubbers, cellulose, etc.), and innovative industrial materials (carbon-based materials, etc.) [28–29].

Examples of hierarchical materials in civil engineering include reinforcing elements of cement mortars or concretes, to be employed for the fabrication of building materials with enhanced strength and fracture toughness [2–4,30]. The longitudinal and transverse profiles of such elements must be adapted to the size of the aggregates, with the aim of obtaining an optimal adhesion between reinforcing fibers and meshes and the matrix material [31].

We deal in the present paper with the design, additive manufacturing and experimental characterization of architectured reinforcing elements for composite materials that exhibit fractal geometry, with a focus on cement matrix composites. The presented study significantly generalizes the research presented in Refs. [2–4] on the additive manufacturing of reinforcing elements with multiscale surface texture, by developing a general design procedure for fibers and meshes that employs the Koch curve concept at different scales [20]. In addition, the present work enriches the results given in [2–4] by investigating the accuracy of the additive manufacturing process in metallic materials applied to the examined reinforcements, and through an experimental study of the influence played by the level of complexity of such elements on the flexural response of a fiber-reinforced mortar. Section 2 of the manuscript illustrates the proposed fractal design algorithm, together with a variety of "Koch" fibers and meshes that it allows to be generated. Next, Section 3 describes a first approach to the AM of physical samples of such reinforcing elements in metallic materials, which consist of reinforcing fibers (or rebars) featuring fractal cross-section boundary, and meshes formed by weaving wires that exhibit fractal longitudinal profile. The examined samples are fabricated in the Ti6Al4V titanium alloy, through electron beam melting (EBM), employing the Arcam EBM Q20 plus facility available at the Department of Materials Science and Engineering of the University of Sheffield. We employ EBM in the present study with the aim of contributing to the active area of research of the cement industry that is oriented to the use of 3D printed metallic reinforcements of construction materials. While we note that this process, and the titanium alloy selected, are relatively high cost compared to current rebar processing technology and materials, developments are being made in Additive Manufacture of metallic reinforcements of construction materials [32] and in the AM processing of large structures for civil engineering in general (such as the 3D printed bridge developed by MX3D, set to be installed in Amsterdam this year [33]), and this work contributes to that area of research. EBM and Ti6Al4V were chosen for this initial study as these are a well-established method and material, meaning that the results are less likely to be influenced by unknown processing factors. Sections 4 and 5 of this paper respectively describe the 3D digitization of the AM samples, and the microstructure characterization of such elements. Mechanical and physical tests on the AM samples are presented in Section 6. The Discussion section (Section 7) examines the potential of such elements when acting as reinforcements of novel mortar and concrete composites. Concluding remarks and directions for future work are outlined in Section 8.

2. Fractal design algorithm for reinforcing fibers and meshes

Fractal fibers and meshes can be designed in a simple and straightforward way through an algorithm based on the Koch curve concept [20–23] and three complexity parameters (or orders) n, m and p. Fig. 1 illustrates the "Koch algorithm" that we employ in the present work. The first complexity parameter n at the basis of this algorithm is related to the fractal dimension of the boundary of the cross-section of the element. This parameter counts the number of self-similar divisions of the equilateral triangle corresponding to $n = 0$, which produce a Koch snowflake in the limit $n \to \infty$ [21]. The second complexity parameter m controls the numbers of the iterations of the Koch curve that we employ on a fixed segment of the longitudinal profile of the fiber (Fig. 1). Finally, the third complexity parameter p counts the numbers of copies of such a segment that we employ along the longitudinal span of the element. We hereafter name Koch fibers the shapes generated according to the algorithm presented in Fig. 1, implicitly intending that such a nomenclature is rigorous only in the limiting cases with $n, m \to \infty$. 3D CAD models of Koch fibers corresponding to different finite complexities n and m (assuming $p = 1$) are given in **Fig. 2**.

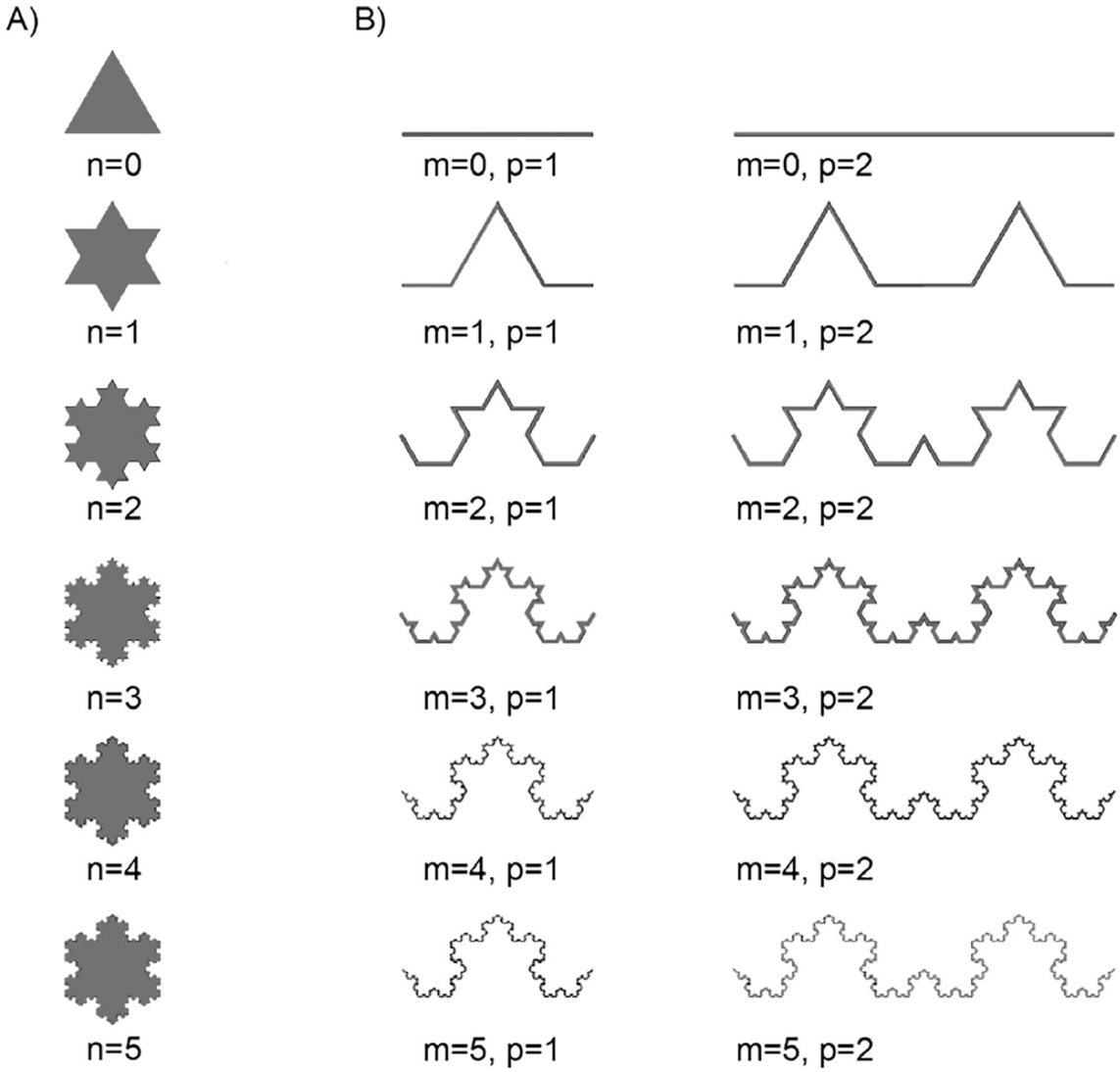

Fig. 1. Fractal algorithm based on the Koch curve and three complexity parameters n, m and p to generate the cross-section (A) and the longitudinal profile (B) of reinforcing elements with fractal geometry.

We refer the reader to Refs. [20–23] for the computation of the fractal measures of the surfaces and lines generated by the algorithm in Fig. 1. For technical purposes, it is useful to introduce two complexity ratios associated with the geometry of the lateral surface of the Koch fibers. The first of these quantities is defined as the ratio between the perimeter of the cross-sections of a Koch fiber and the circumference of a circle having same area (*transverse complexity ratio*). The second complexity ratio instead relates the length of the longitudinal profile of a Koch fiber for $m > 0$ with the length of the rectilinear segment corresponding to $m = 0$ (*longitudinal complexity ratio*). Table 1 shows the complexity ratios of Koch fibers featuring different orders n and m. For $n = m = 3$, it is observed that the Koch fiber has cross-section perimeter 2.45 times larger than the perimeter of a circular fiber with equal cross-section area. The same fiber has also longitudinal length 2.37 times larger than the length of a straight fiber. This implies that the measure of the lateral surface of the Koch fiber under consideration is equal to (2.45×2.37) 5.81 times the measure of the lateral surface of a circular cylinder of equal volume. Similar but less pronounced results are obtained for lower values of the orders n and m (cf. Table 1).

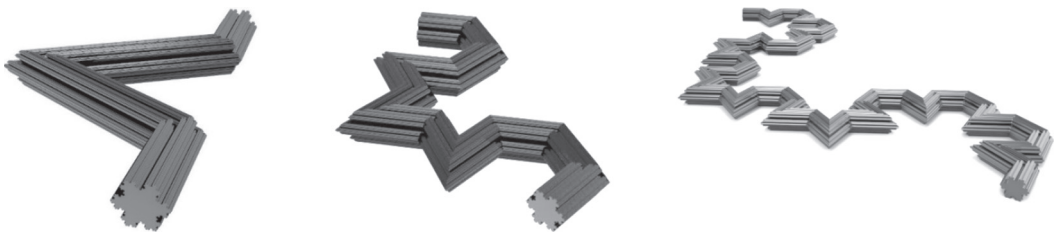

n=5, m=1 *n=5, m=2* *m=n=3*

Fig. 2. 3D views of Koch fibers for different complexities.

Table 1
Complexity ratios of Koch fibers (L denotes one third of the length of the closed/open line segment corresponding to $n = 0/m = 0$).

n	Cross-section perimeter	Cross-section area	Transverse complexity ratio
0	03.00 L	0.4330 L2	1.29
1	14.00 L	0.5773 L2	1.49
2	25.33 L	0.6415 L2	1.88
3	37.11 L	0.6700 L2	2.45
m	Fiber length		Longitudinal complexity ratio
0	01.00 L		1.00
1	11.33 L		1.33
2	21.78 L		1.78
3	32.37 L		2.37

The Koch algorithm illustrated so far can be generalized in a number of ways, in order to suitably design a large variety of fractal fibers and meshes, which fit different technical applications. A first generalization of the basic Koch algorithm is obtained by recourse to the (q,c)-Koch curve concept [21]: starting with a regular polygon of side L, one can replace the middle cL portion of the generic side with a regular polygon featuring q sides, c denoting a positive number <1. Such a division process can be recursively applied to the segments of the newly generated polygon, creating a fractal shape. Fig. 3a shows three iterations of such a construction, for $q = 6$ and $c = 1/3$. The second generalization of the Koch algorithm regards the directionality of the division process, that is the side towards which the recursive divisions of the edges of the Koch curve are applied. The subdivision "side" can be suitably switched during the division process on selected portions of the Koch curve, giving rise to "balanced" fractal profiles (facing partially upward and partially downward). A third generalization is concerned with the possibility to join segments of (q,c)-curves corresponding to different values of q and c and different complexities, in order to form "composite" fractal shapes. Such a joining process can also make use of rotations and folding of the above segments, and may profit from the random composition of fractal shapes. Fig. 3b shows the longitudinal profile of

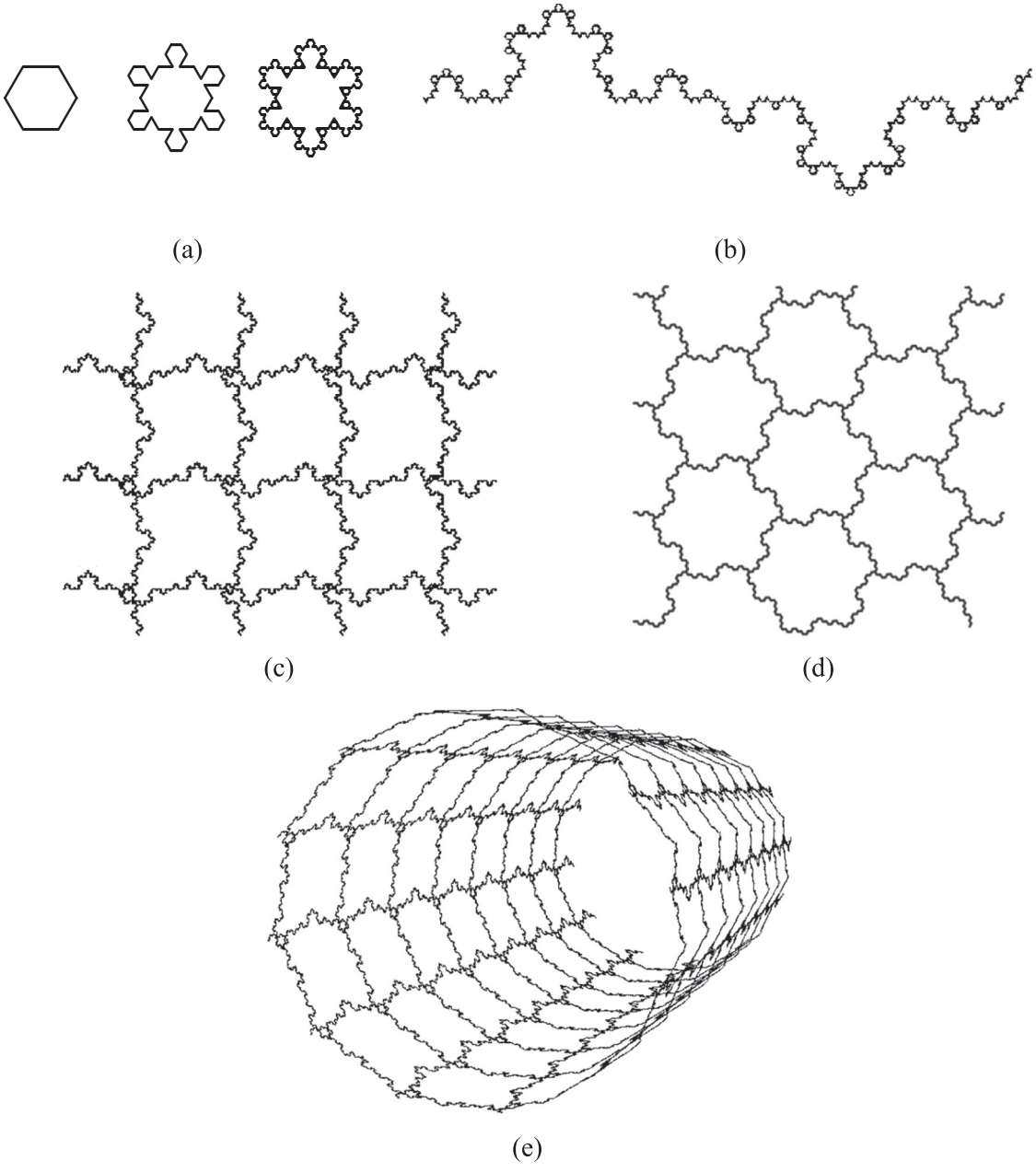

Fig. 3. Composite Koch fibers and meshes.

a composite Koch fiber, while Fig. 3c and d show meshes obtained by crossing composite Koch fibers. Finally, Fig. 3e shows a cylinder obtained by rolling a Koch mesh along a side. It is worth observing that the transverse diameter of the generic edge of a Koch fiber cannot exceed its longitudinal length, which introduces a dependence of the transverse scale of the fiber over the longitudinal scale. The hierarchical organization of the interface between a Koch reinforcement and the surrounding matrix material is discussed in Section 0.

3. Additive manufacturing of physical samples

Due to the technological challenge of additively manufacturing fine-scale hierarchical Koch fibers in metallic material, in this study we focus our attention on the fabrication of Koch fibers of the following simple types: Koch fibers (or bars) with straight longitudinal profile and fractal cross-section, for varying complexities *n*, and a Koch mesh formed by a grid of composite Koch fibers with circular cross-section and fractal longitudinal profile.

Fig. 4 shows the CAD models and AM samples of the analyzed fibers, which include a square fiber with edge length $L_0 = 5.32$ mm (labeled KF0), and three Koch fibers KF1, KF2 and KF3. The latter are obtained by applying the Koch algorithm with complexity *n* equal to 1, 2 and 3, respectively, to the sides of squares with edge lengths $L_{01} = 5.05$ mm, $L_{02} = 4.98$ mm, and $L_{03} = 4.95$ mm. The distance between two successive vertices of the KFn cross-section boundary is computed as follows: $L_n = (1/3)^n L_{0n}$ [21,22], and it is easily verified that it results in $L_1 = 1.68$ mm, $L_2 = 0.55$ mm, and $L_3 = 0.18$ mm. The last two of these lengths approach the resolution limits for processing by this technique in metal; it has been reported that the dimensions of heat sources used in AM fall within this range [30]. All the examined fibers exhibit equal cross-sectional area $A = 28.35$ mm^2, and 160 mm length (giving the volume: $V_{KF} = 4536$ mm^3), which correspond to 6.01 mm equivalent diameter. The morphology of the cross section of the 3D printed bar KF3 is illustrated in Fig. 5. The image in Fig. 5 and the microstructure characterization presented in Section 5 employ an optical microscope (OM) Nikon eclipse LV150 with crossed polarized light imaging capability.

The examined meshes are illustrated in Fig. 6. A simple rectangular mesh (RM) with 8.11 mm × 11.79 mm spacing and cylindrical wires of 0.86 mm diameter is analyzed in comparison with a Koch mesh (KM). The latter is equipped with composite Koch wires featuring cylindrical cross-section with 0.59 mm diameter, and a fractal longitudinal profile. The distance between consecutive vertices of such a profile ranges from a maximum value of 1.12 mm down to a minimum value of 0.17 mm. The width of the RM and KM samples is 35 mm, while their length is 155 mm. The total volume of the Koch mesh is $V_{KM} = 624.92$ mm^3, while that of the square mesh is $V_{RM} = 628.93$ mm^3. We refer the reader to Fig. 6 for a graphical illustration of the architecture of the Koch mesh.

Additive Manufacturing processes often produce samples with anisotropy in their underlying defect structure and microstructure, due to the directional way the material is built up. Here STL files (provided in the Appendix) were orientated in such a way to additively manufacture the samples they defined at the best possible resolution and with the lowest possible concentration of defects. To do this, an orientation parallel to the build direction was used for rods and an orientation at 45° to the build direction for mesh samples; the latter configuration was intended to avoid preferential defect location in thin members [31]. All samples were manufactured using a Q20 plus ARCAM system with prealloyed Ti-6Al-4 V plasma atomised powder deposited in 50 μm thick layers, using the process parameters described in the Appendix. We additively manufactured nine samples of each analyzed fiber

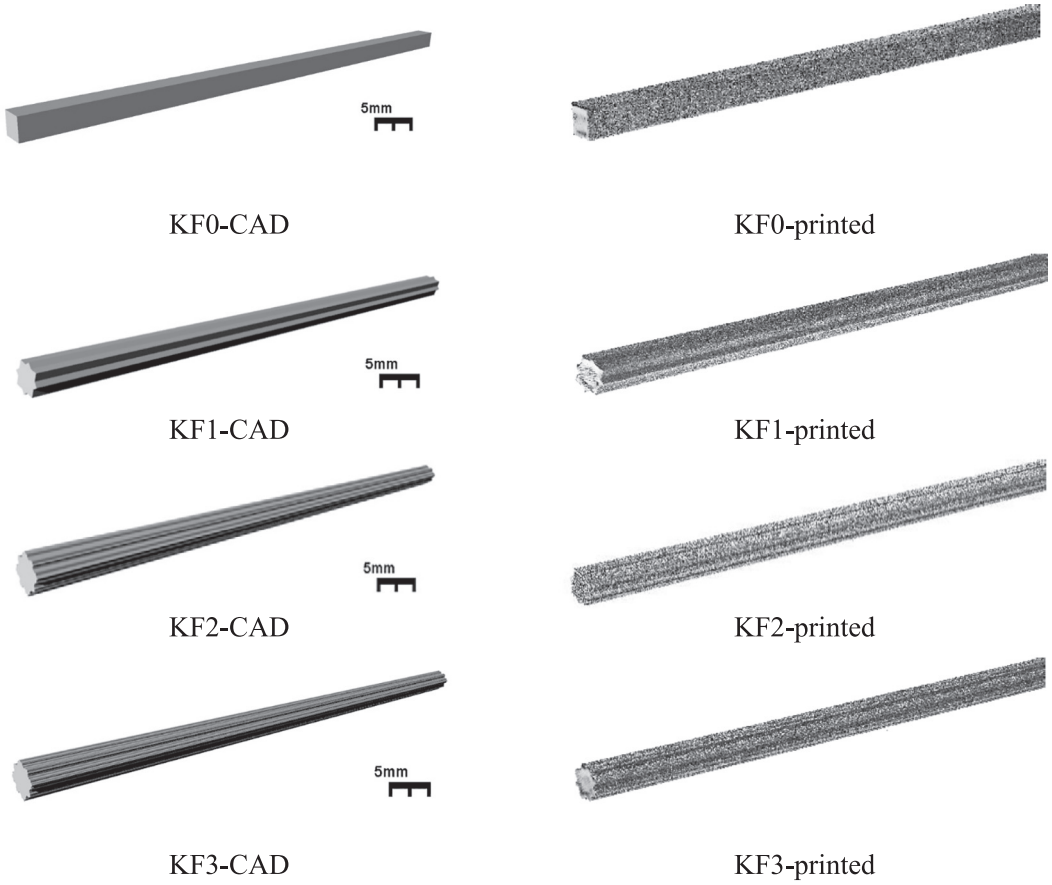

Fig. 4. CAD models and 3D printed samples of the analyzed Koch fibers.

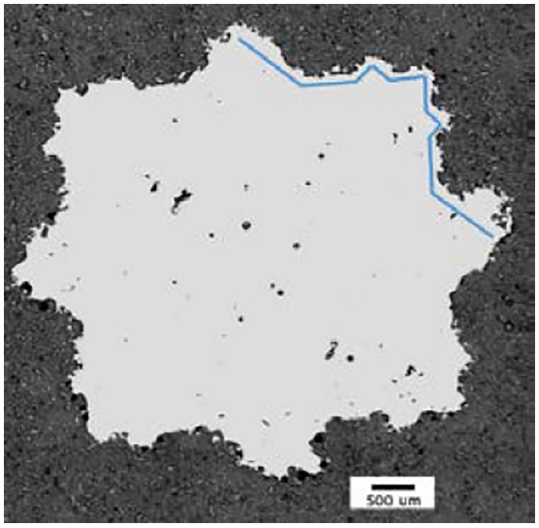

Fig. 5. Optical microscope image showing the "as-built" cross section of Koch bar KF3 with an equivalent diameter of 6.01 ± 0.2 mm. Blue insert bars representing regions of KF2 bar are shown for reference. (For interpretation of the references to color in this figure legend, the reader is referred to the web version of this article.)

and mesh. Careful examination of the samples produced was needed, since the size of the EBM-built objects can be affected by the inherent surface roughness (and its effect on resolution) if manufacturing fine features is attempted, or by solidification shrinkage effects for larger ones. When compared with the CAD models the actual dimensions may therefore vary. As mentioned before, minimum achievable feature sizes in this system of ~0.4 mm are estimated based on similar findings in literature [30–40]. With such variances from the design, we accept that the AM samples of the Koch fibers and the Koch mesh do not exactly match the theoretical geometries described above, especially in the case of the KF3 fiber and the Koch mesh KM (see Fig. 4); the issue of the accuracy of the AM parts is addressed in the next section of the manuscript.

4. 3D laser scanner surveys

The accuracy of the employed Additive Manufacturing process was assessed by measuring the deviations between the geometry of an AM specimen and that of the corresponding master CAD model, for all the samples illustrated in Figs. 4 and 6. Such a graphical comparison test was conducted by capturing the 3D shape of each EBM-built object through a 3D digitizer. The small features exhibited by the examined fibers and meshes (cf. Section 3) were captured through the non-contact 3D scanner VIVID 910 by Konica Minolta [41–42]. After the scanning of the 3D printed parts, the digitized images produced by the VIVID 910 built-in software (cf. the Appendix) were exported to the STL format. The digitized STL (DSTL) mesh of each analyzed object was next imported into the Geomagic Studio 2014 software [43], together with the STL file of the CAD drawing (CSTL). The first phase of the graphical comparison test consisted of the alignment between the DSTL and CSTL models. Such a process was divided into two steps: a first rough alignment based on point picking, followed by a best-fit alignment obtained through an iterative closest point algorithm [41], always taking the CSTL model as reference. The second phase resulted in the generation of three-dimensional, color-coded maps of the deviations observed between the positions of the parent vertices of the DSTL and CSTL models, which were determined through the algorithm illustrated in the Appendix.

Table 2 illustrates the statistics of the tests run between the examined DSTL and CSTL models. It is worth observing that the distances between parent vertices of the such models can be either positive or negative, being oriented along the outward normal to the external surface of the CSTL model (cf. the Appendix). In the case of the Koch fibers and meshes, the rightmost column of Table 2 gives the relative error defined by the ratio between the Root Mean Square (RMS) deviation between CSTL and DSTL models and the minimum CSTL feature (minimum distance between adjacent vertices).

The color maps of the oriented distance errors between the CSTL and DSTL models of the KF2 bar and the Koch mesh KM are reported in Figs. 7 and 8, respectively. The analogous maps relative to the KF1 and KF3 bars are provided in the Appendix. The results in Table 2 highlight that the minimum deviations between the CSTL and DSTL models are observed with reference to the KF0 fiber (cf. Fig. 7). The fractal fibers KF1 and KF2 show greater RMS errors and relative errors, as compared to KF0. Finally, the KF3 fiber and the fractal mesh KM exhibit smaller RMS errors and greater relative errors over the KF1 and KF2 fibers. The maximum CSTL-DSTL deviations were observed in correspondence with the folds of the AM objects (cf. Figs. 7, 8 and the Appendix). It is worth noting that the relative errors associated with the KF3 (90.05%) and KM (75.99%) elements are markedly high, since the oriented distances between the CSTL and DSTL vertices of such objects are of the same order of magnitude as the size of the minimum features of the CSTL models. We recall that the KF3 bar and the KM grid display minimum features of the order of 0.2 mm, which go markedly below the minimum achievable feature sizes of the employed ARCAM EBM facility (~0.4 mm), as we already observed in Section 3. Overall, the results in Table 2 reveal that an accurate additive manufacturing of the Koch fibers and meshes exhibiting high complexity calls for the adoption of equipment with higher accuracy than the ARCAM Q20 facility employed in the current work.

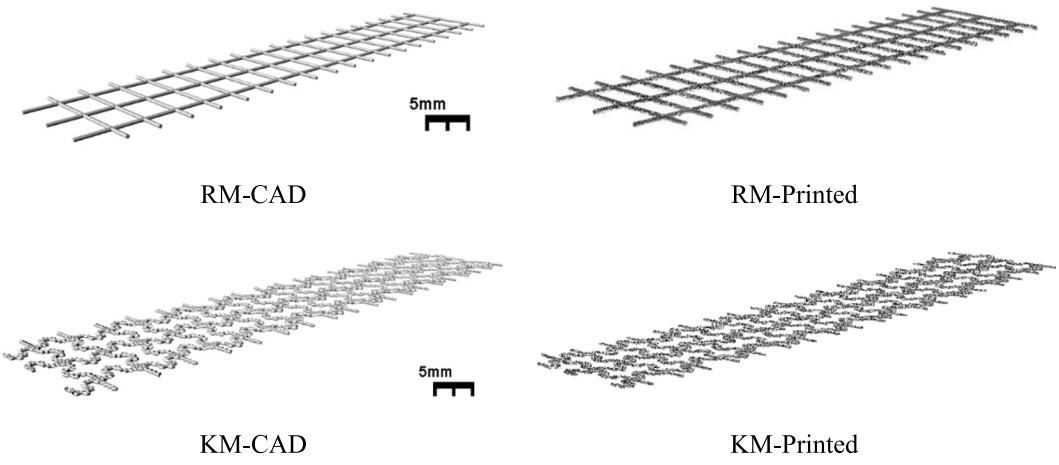

Fig. 6. CAD models and 3D printed samples of a rectangular mesh (RM) and a Koch mesh (KM).

Table 2
Statistics of the graphical comparison tests between CSTL and DSTL models.

Object	Max. distance + (mm)	Max. distance − (mm)	Average distance (mm)	Average distance + (mm)	Average distance − (mm)	Standard deviation (mm)	RMS estimate (mm)	Min. feature (mm)	Relative error (%)
KF0	0.51	−0.40	0.05	0.10	−0.05	0.10	0.11	5.33	2.06
KF1	0.65	−0.83	−0.06	0.10	−0.16	0.17	0.18	1.68	10.51
KF2	0.76	−0.79	−0.07	0.17	−0.20	0.22	0.23	0.55	41.83
KF3	0.81	−0.51	0.02	0.14	−0.11	0.16	0.17	0.18	90.05
KM	0.72	−0.54	0.07	0.11	−0.07	0.11	0.13	0.17	75.99

5. Microstructure characterization

The "as-built" material microstructure was characterized through optical microscopy. Sample preparation began by cutting the material, which was then mounted in bakelite for further surface preparation, using standard methods which are described elsewhere [30]. The observations under OM showed a microstructure composed of a fine plate morphology and traces of columnar grains, see Fig. 9. This type of microstructure in α + β Ti-6Al-4 V titanium alloy produced by EBM has been reported extensively in previous work in the field [34–35].

The microstructural features observed (both here and in earlier work) develop from the first columnar grains (β-phase) which form immediately on solidification. On cooling to room temperature there is a transformation to an α + β microstructure, with some of the prior microstructure remaining visible, accompanied by α-phase formed by the allotropic transformation. As the cooling rates are relatively fast in AM processes [36], the transformation is rapid and diffusionless, and the microstructure developed is in the form of fine plates, with their thickness reported to be inversely proportional to the cooling rate. The mechanical properties of Ti6Al4V have been reported extensively in terms of their variation with this plate size [37]. Fine grain morphologies (effectively the case if the plates are small) impede the motion of dislocations going through the material, and so finer microstructures are usually correlated with high resistance to permanent deformation [37]. In this work, fine plate microstructures can be observed from bar and mesh samples, see Fig. 9.

6. Mechanical and physical tests

6.1. Vickers hardness

Although quantification of the length scale in relation to dislocation motion in these complex microstructures is not straightforward, Vickers hardness values of bar and mesh samples are shown in Fig. 10. Vickers hardness was carried out using a Struers Durascan 70 automated indenter. Prepared surfaces used for metallographic observations were indented with 0.1 kg of load in 10 × 10 arrays with 0.1 mm spacing and 5 s of dwell time. It can be seen that mesh samples show relatively higher hardness values, suggesting higher strength properties in general (approximately ~1030 MPa, as the hardness of metals can be related in a general way to yield strength [38]), due to the faster cooling rates [39] which are easily generated in such low thermal mass components.

6.2. Contact angle tests

Contact angles tests have been run on the AM fibers shown in Fig. 4 in order to study the interaction of the surface roughness induced by the EBM deposition process [30] with the fractal geometry of such elements. It is well known that contact angle tests executed on sessile liquid drops deposited on a solid surface allow for an effective and easy characterization of the surface through its wettability (refer, e.g., to [40–46] and references therein). Different results are obtained when running such tests on smooth and rough surfaces, since the apparent (or experimental) contact angle ϑ^* of the deposited liquid drop on a non-smooth surface is strongly affected by the surface roughness and the phenomenon of contact angle hysteresis [40–46].

We performed ten optical contact angle tests on the fibers shown in Fig. 4, through the OCA System 20 apparatus distributed by DataPhysics Instruments [47]. Such tests were carried out by dropping 1 μl water drops on the lateral surface of the fiber. The mean values and standard deviations of the contact angle measurements are provided in Table 3 (see the Appendix for the pin-sharp drop images recorded for the samples under testing). The results in Table 3 highlight that all the measured contact angles are >90°, and that the mean value of ϑ^* is slightly greater for the Koch fibers KF1, KF2 and KF3, than the square fiber KF0. In particular the mean value of ϑ^* for KF3 is only 3.5% different from the mean value of the same quantity referred to the square fiber KF0. We are led to conclude that the surface roughness of the AM Koch fibers is

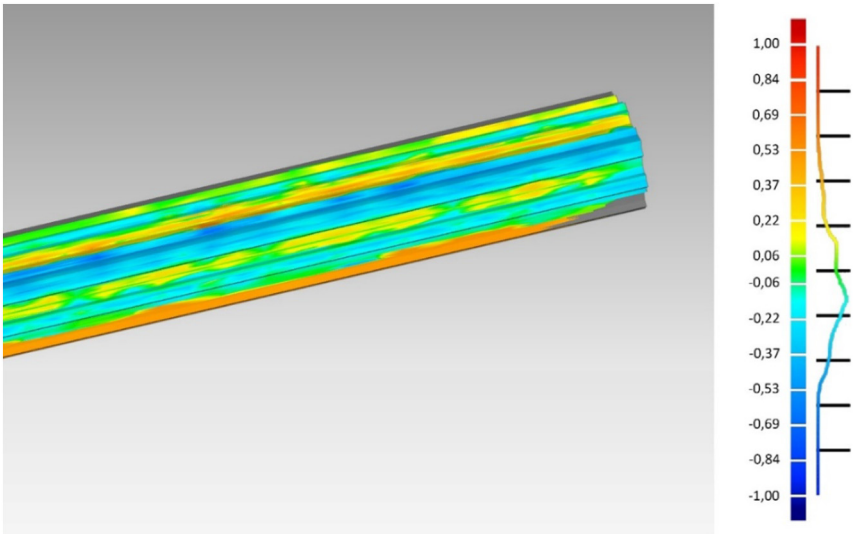

Fig. 7. GC test on the Koch bar KF2: ±max = 0,76/−0,79 mm; ±average = 0,17/−0,20 mm; standard deviation = 0,22 mm; RMS estimate = 0,23 mm.

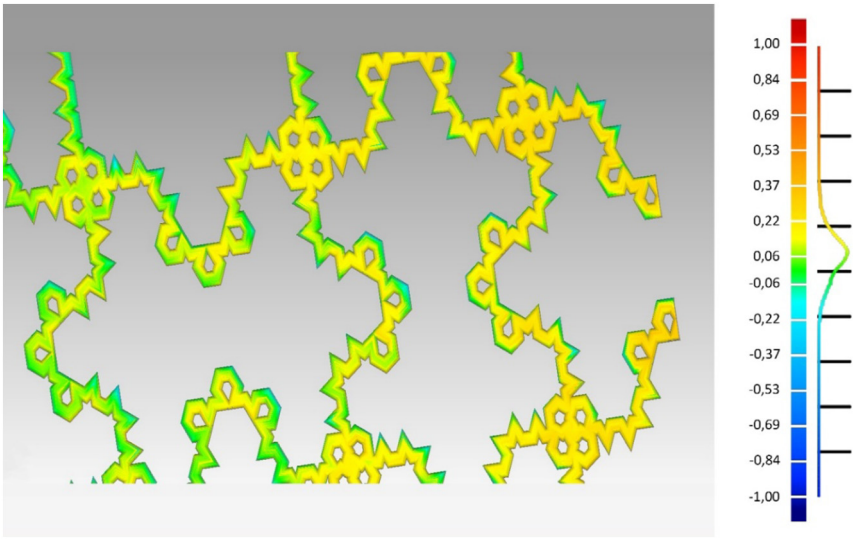

Fig. 8. GC test on the Koch mesh KM: ±max = 0,72/−0,54 mm; ±average = 0,11/−0,07 mm; standard deviation = 0,11 mm; RMS estimate = 0,13 mm.

not dramatically affected by the fractal geometry in the design of such elements. This in turn implies that the EBM deposition process (i.e. powder raw materials used), influences and retains, up to some point, a surface performance when processing parts with the geometries of the Koch fibers.

6.3. Bending tests on mortar specimens reinforced with Koch fibers

We conducted a study on the strengthening ability of the reinforcements analyzed in the present study by running three-point bending tests on prismatic 40 mm × 40 mm × 160 mm mortar specimens reinforced with KF0, KF1 and KF2 fibers/bars. The European standard EN 1015-11:2007 [48] was employed to run such tests, using a MATEST electrically operated testing machine with 200 kN capacity [49]. The KF3 bars and the KM grid illustrated in Section 3 were not included in the present study, due to the limitations of the employed EBM technology in manufacturing parts with minimum feature sizes. As we already noted in Section 4, these limitations are determined by factors such as the heat source spot size and powder size distribution.

We analyzed a mortar that employs 80% (weight) Portland cement and 20% fly ashes as binders, in association with 80% ground granulated blast furnace slag and 20% marble slag as aggregates (water/binder ratio equal to 50%). Such industrial by-products provide economic and environmental benefits and enhance cohesiveness of the matrix [50–51]. The fine-size marble slag filler indeed minimizes the internal friction and facilitates the particle distribution, leading to improved workability of the mixture. The mix design of the employed mortar is illustrated in Table 4. Mortar specimens were cast in 160 × 40 × 40 mm molds with embedded fractal rebars. The molds were filled in two stages. In the first stage, a layer of mortar was poured up to 12 mm height (net mortar cover of the fibers), making use of a mechanical mixer. Next, the reinforcing bars were placed into the mold, and additional mortar was poured until the mold was filled. The mortar was compacted using a mechanical mixer and the specimen was leveled with a trowel. Finally, the specimens were cured while sealed within the molds at 40 °C for 24 h, and unsealed, after mold removal, for additional 27 days at room temperature before testing.

The mechanical characterization of the unreinforced (UNR) mortar was carried out by testing four cubic specimens with 40 mm edge length. Ultrasonic tests conducted through a portable ultrasonic nondestructive tester (test procedure illustrated in [52]) lead us to estimate the following mean value of the dynamic modulus of elasticity of the mortar: E_{dm} = 14.29 GPa, (5.97 GPa standard deviation), while uniaxial compression tests estimated a mean compressive strength f_{cm} = 14.50 MPa (4.68 MPa standard deviation). We reinforced three different mortar specimens with AM processed exemplars of the KF0, KF1 and

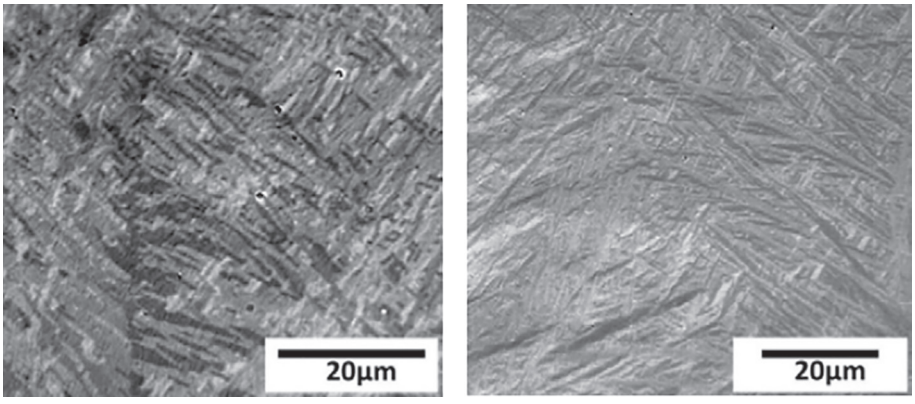

Fig. 9. Microstructural morphology composed of fine alpha plates. (a) KF3 sample in the build direction showing columnar grain boundaries and α-plates. (b) Fractal mesh sample showing fine α-plates.

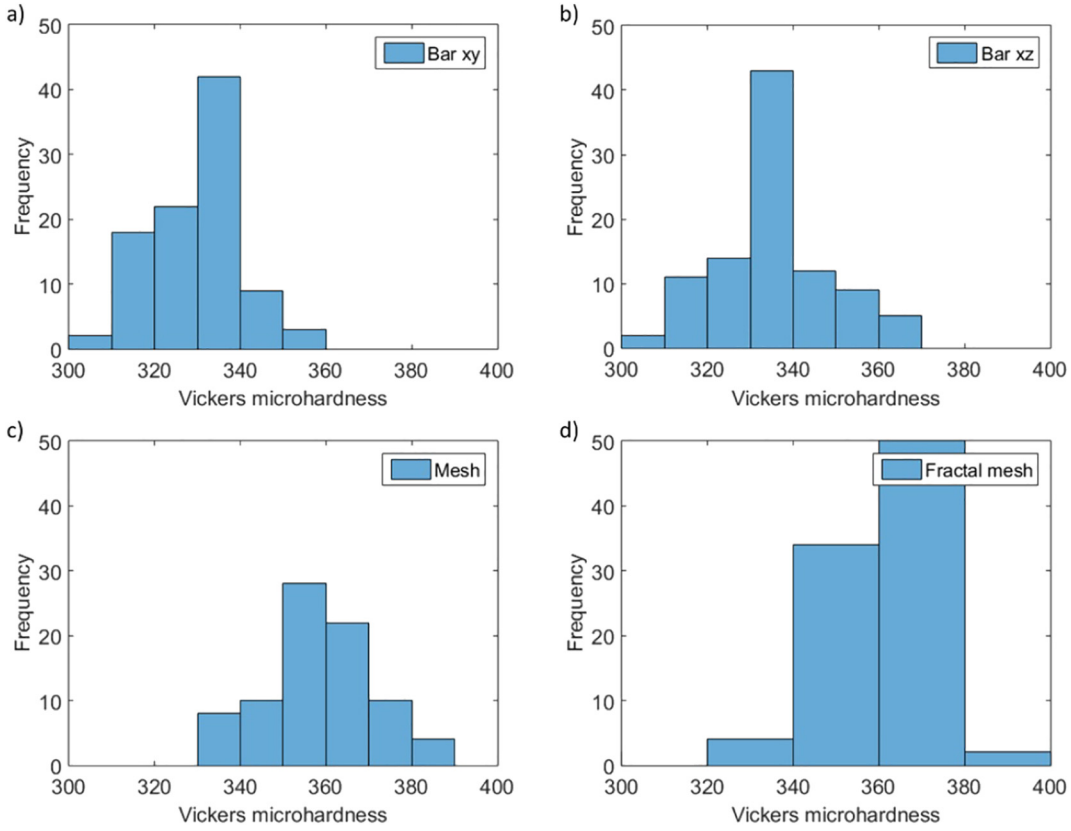

Fig. 10. Histograms showing Vickers microhardness values from; (a) KF3 bar sample in cross sectional area; (b) KF3 in the build direction; (c) RM sample; (d) KM sample.

KF2 fibers, and, in addition, conducted bending tests also on three unreinforced mortar specimens. The three-point bending tests were executed on a clear length $L = 100$ mm, using a 0.50 mm/min loading rate.

Let F and δ respectively indicate the transverse force applied at the center of the specimen and the midspan deflection, and let $\sigma = \frac{3}{2}\frac{FL}{a^3}$ denote a reference axial stress, which corresponds to the stress acting at the extreme fibers of the cross-section in the uncracked regime. The F vs. δ and σ vs. δ responses of all the analyzed specimens are graphically illustrated in Fig. 11, while pictures taken during and after the bending tests on selected specimens are presented in Fig. 12. The F-δ and σ-δ curves shown in Fig. 11 exhibit an initial linear branch for small values of δ, which is followed by a nonlinear branch exhibiting progressively decreasing slope. Such a branch terminates with critical points $C \equiv (\delta_{cr}, F_{cr})$ and $C' \equiv (\delta_{cr}, \sigma_{cr})$, where the F vs. δ and σ vs. δ curves exhibit marked force and stress drops, respectively, due to the onset of a macroscopic crack at the bottom edge of the specimen near the midspan. The post-critical behavior is characterized by a nearly horizontal plateau of the above curves, describing the response of the fractured material. This mechanical behavior originates from the formation of diagonal cracks at the supports (typically at one support, as in most of the present examples, but possibly also at both supports), which add to the initial crack, and are accompanied by subsequent additional cracks in the region between the midspan and the supports. The described crack pattern leads to the diffuse crushing of the mortar, and finally to failure of the material (cf. Fig. 12). The statistics of the bending tests are given in Table 5, where F_{cr} denotes the value of F at the critical point; $f_{lf} = \sigma_{cr}$ denotes the first crack strength of the material; and F_{res} denotes the average value of the residual load-carrying capacity in the loading interval between $\delta = \delta_{cr}$ and $\delta = 5$ mm. Referring to the average values, one observes 154% and 31% increases of F_{cr} and f_{lf} in KF2-reinforced specimens, over UNR and KF0 samples, respectively. The value of F_{res} in KF2 specimens is 37% higher than that exhibited by KF0 samples, while such a quantity is practically zero in the unreinforced mortar (Fig. 11). Significant increases in the average of F_{cr}, f_{lf} and F_{res} are also observed when passing from KF2 to KF1 specimens (cf. Table 5).

With reference to cement matrix composite structures loaded in bending, there is a large body of experimental evidence that the response of the tension tie-rods active in such structures is characterized by the bond behavior, affected by adhesion, friction and interlocking [53–55]. The rebar-matrix slip law initially shows a linear shape, as long as the adhesion between such elements prevails over friction and interlocking. This initial response is followed by a nonlinear branch of the tangential stress (tau) vs. slip curve, due to the onset of more significant bar-matrix slipping. The nonlinear branch is associated with the micro- and macro-cracking of the interface, and appreciable

Table 3
Mean values and standard deviations of the contact angle measurements.

Fiber-type	ϑ^* (°) Mean ± St.Dev.
KF0	109.3 ± 7.6
KF1	109.6 ± 6.9
KF2	112.9 ± 6.8
KF3	113.1 ± 7.7

Table 4
Mix-design of the employed mortar specimens.

Component	Dosage
Portland cement (binder)	360 g
Fly ash (binder)	90
Ground granulated blast furnace slag (aggregate)	1080 g
Marble slag (aggregate)	270 g
Water	225 g

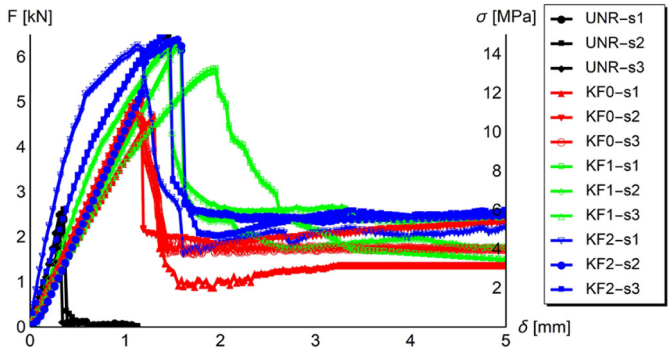

Fig. 11. Force- and stress-deflection curves of the unreinforced mortar specimens (UNR), and the specimens reinforced with KF0, KF1 and KF2 fibers.

interlocking and friction effects. The peak of the tau-slip curve marks a critical equilibrium point, which is followed by a softening response of the material up to failure, due to the spalling of the matrix produced

Table 5
Experimental values of the peak load (F_{cr}), the midspan deflection (δ_{cr}) corresponding to F_{cr}, the first crack strength (f_{lf}), and the residual load (F_{res}) measured during bending tests.

Material	Specimen	F_{cr} [kN]	δ_{cr} [mm]	f_{lf} [MPa]	F_{res} [kN]
UNR	s1	2.39	0.35	5.59	–
	s2	2.56	0.35	6.02	–
	s3	2.48	0.31	5.82	
	avg	**2,48**	**0.34**	**5.81**	–
KF0	s1	4.62	1.30	10.84	1.33
	s2	4.99	1.14	11.70	2.10
	s3	4.70	1.09	11–02	2.36
	avg	**4.77**	**1.18**	**11.18**	**1.93**
KF1	s1	5.65	1.95	13.25	2.39
	s2	6.14	1.45	14.41	2.05
	s3	6.17	1.53	14.45	2.59
	avg	**5.99**	**1.64**	**14.03**	**2.34**
KF2	s1	6.44	1.44	15.10	2.45
	s2	6.18	1.13	14.49	2.24
	s3	6.30	1.55	14.76	2.49
	avg	**6.31**	**1.37**	**14.78**	**2.39**

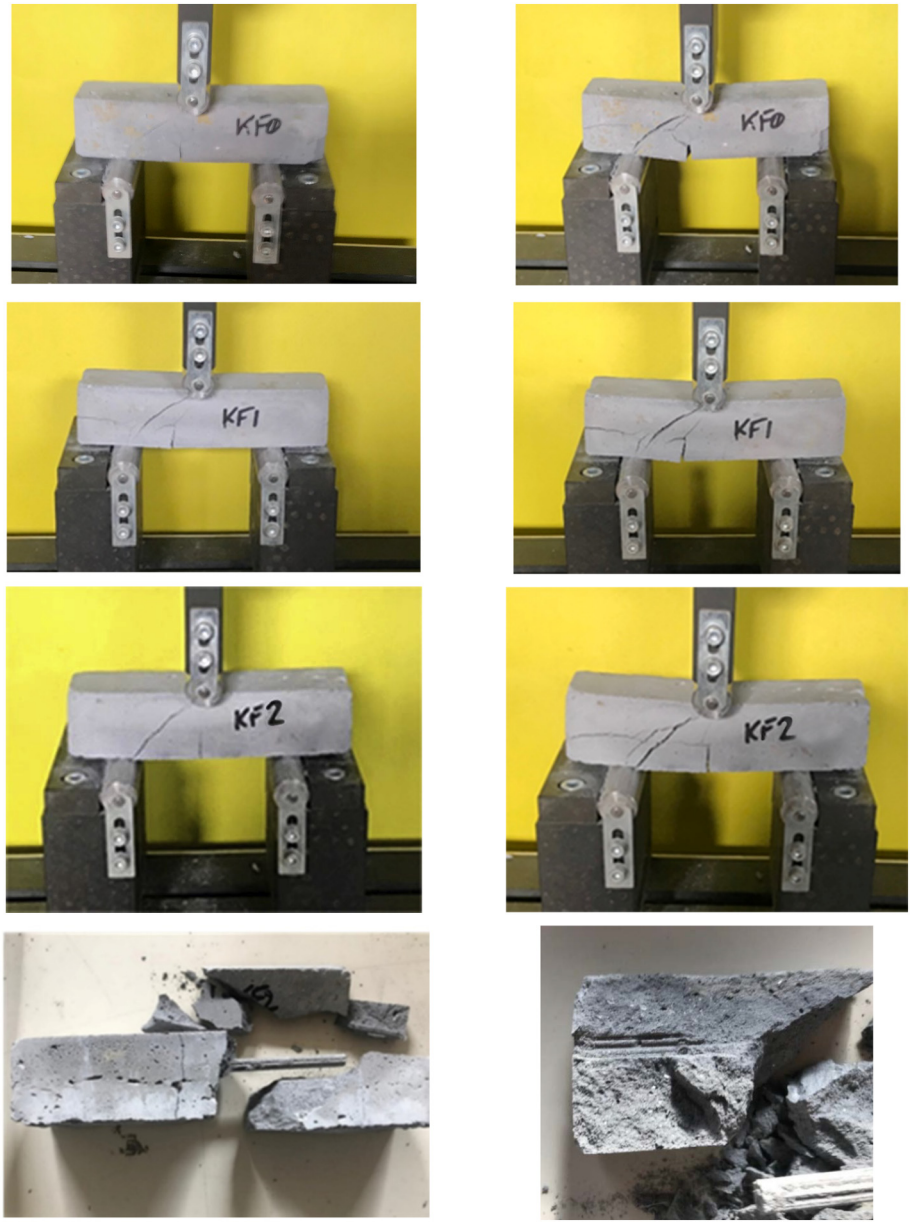

Fig. 12. Pictures taken during the bending tests on selected specimens (top), and after the failure of a KF2 sample (bottom).

by the ribs of the rebars (see, e.g., [55] and references therein). The tie-rod response in presence of appreciable interlocking effects is markedly influenced by the texture of the rebars [53–56]. Some different failure modes may also occur, due, e.g., to pull-out failure, bar rupture, concrete cover failure, etc., which are not of interest in the present case [56].

The visual inspection of the experimental response of the mortar specimens analyzed in the present study confirms the above experimental findings, and highlights that such specimens exhibit a strut-and-tie mechanism in the fracture regime [57]. This resisting mechanism is formed by compressed diagonals, a top chord member, and a bottom tension-tie rod (cf. Fig. 12). In particular, one observes that the $F-\delta$ response of the KF0 specimens exhibits a nearly linear profile up to the critical point (Fig. 11), which means that the strut-and-tie mechanism is mainly effective only in the post-critical regime in the present case (cf. Fig. 12-top). By contrast, the $F-\delta$ curves of the KF1 and KF2 specimens show a markedly nonlinear shape before the critical force drop occurs, due to the onset of significant slipping and interlocking phenomena already occurring under the pre-critical conditions (Fig. 12-center/bottom).

A theoretical estimate of F_{cr} can be obtained by assuming perfect adhesion between the reinforcing fiber and the mortar in the pre-critical regime, making use of the following formula for the maximum tensile stress supported by the undamaged material [2].

$$f_t = \frac{F_{cr} L/4}{I}(a-x). \tag{1}$$

In Eq. (1), I is the moment of inertia of the full-resistant cross-section, and x is the depth of the neutral axis. The adoption of standard homogenization techniques [58] leads us to predict

$$x = \frac{n\,A_b + n' a^2}{a\,(1-n')}\left[-1+\sqrt{1+\frac{2\,a\,(1-n')\,(n\,A_b d + n' a^3/2)}{(n\,A_b + n' a^2)^2}}\right], \tag{2}$$

$$I = \frac{a}{3}\left[x^3 + n'(a-x)^3\right] + n\,A_b (d-x)^2. \tag{3}$$

where n denotes the ratio between the Young modulus of the bars E_b and the Young modulus of the mortar in compression E_{cm}; n' denotes the ratio between the Young modulus of the mortar in tension E_{tm} and E_{cm}; A_b indicates the cross-section area of the bar; and d denotes the effective depth of the cross-section. Let us now assume $E_{cm} \cong E_{dm}$, $A_b = 28.35\ \text{mm}^2$ (cf. Section 3), $f_t = 5.81\text{MPa}$ (cf. Table 5), $d = 24.50$ mm, and $n' = 0.5$. The use of such assumptions in Eqs. (1)–(3) lead us to the following results.

$$x = 5.56\text{mm}, I = 3,55 \times 10^5\ \text{mm}^3, F_{cr} = 4.80\ \text{kN}. \tag{4}$$

The value of F_{cr} given by Eq. (4) is rather close to the average value of the first crack load in KF0 specimens (4.81 kN cf. Table 5). Such a noticeable result is line with the observation that the $F-\delta$ response of KF0 specimens is almost linear up to the critical point. The higher values of F_{cr} observed in KF1 (5.90 kN) and KF2 (6.31 kN) specimens are instead associated with a markedly nonlinear pre-critical response (Fig. 11). As we already observed, this nonlinear response is explained by the occurrence of pre-critical slipping and interlocking between the Koch fibers and the mortar (cf. Fig. 12-center/bottom).

7. Discussion

We have presented a general purpose methodology for the design of reinforcing fibers and meshes of cement-matrix composite materials with fractal architecture, through suitable manipulation of the Koch curve construction (Section 2). The analyzed reinforcements are aimed at inducing multiscale interlocking phenomena at the interface with the matrix material, due to their complex and multiscale geometry. We observe, indeed, that such elements can be regarded as hierarchical joints between different portions of the matrix, which feature fractal geometry at different levels [24–26]. A first level of hierarchical organization of the Koch fiber – matrix interface naturally arises by the superimposition of the fractal complexity n of the perimeter of the cross-section of the fiber over the complexity m of the longitudinal profile. Other levels of hierarchy may originate from the superimposition of the longitudinal complexities associated with the parameters m and p, as well us from the superimpositions of nested fractal shapes over given segments of composite Koch fibers.

The proposed design approach of reinforcing fibers and meshes mutates ideas from the fractal modeling of fractures and joints in biological systems and architecture materials [24–26], being aimed at creating matrix-reinforcement interfaces with complex geometry. Fig. 13 shows a composite tooth modeling of the interface between a composite Koch fiber and the surrounding matrix material [25]. The fractal geometry and the hierarchical organization of such an interface induce complex load-transmission mechanisms between the teeth associated with the different levels of hierarchy, involving both tension and shear stresses at the tooth-matrix interface.

By extending available results on the mechanics of fractal joints to Koch fiber-matrix interfaces, we expect that the tensile and shear strengths of composite materials reinforced through such elements will strongly depend on the complexities n, m and p of the Koch fibers. We also envisage that such quantities grow with increasing values of the complexity parameters, as a result of the increase in the fiber-matrix contact area [24–26]. Finally, we expect that the thickness of the interface layer decreases for increasing complexities n, m and p, and that rough fracture surfaces may enucleate and propagate in correspondence to such a layer under external loading, producing enhanced surface energy dissipation [2–4,11].

Some preliminary results on the bending response of cement mortar specimens reinforced with Koch fibers have shown that the corrugated geometry of such reinforcements positively influences the bending and shearing response of the tie-rod acting at the tensioned edge of the specimen (Section 6.3). The interlocking mechanisms occurring between the matrix and the “fractal” ribs of the Koch fibers have demonstrated the ability to appreciably increase both the first crack strength and the post-critical load carrying capacity of the material. In terms of the first crack strength of the fiber-reinforced mortar, the results presented in Section 6.3 have demonstrated that mortar specimens reinforced with KF2 fibers exhibit a 152% increase of this property over the unreinforced material, while specimens reinforced with KF1 and KF0 fibers respectively exhibit 141% and 92% increases of the first crack strength, always comparing with the unreinforced material. It is worth noting that research has recently been presented in the literature on the reinforcement of different cement mortars with 3D printed Ti6Al4V cylindrical bars, which have 7.00 mm diameter and are coated with a 0.75 mm × 0.75 mm grid of cylindrical embossments [2–3]. This work showed a 124% increase of the first crack strength of the fiber reinforced material in the case of a low-strength cement mortar (flexural strength equal to 1.00 MPa) [2], and a 97% increase of the first crack strength in the case of the fiber reinforcement of a high strength cement mortar (flexural strength of the unreinforced mortar equal to 8.67 MPa) [3]. We are led to conclude that the fractal geometry of the reinforcing bars examined in the present study appears to be more effective than an embossed geometry, as far as it concerns the enhancement of the flexural strength of the fiber-reinforced mortar, due to marked interlocking effects at the fiber-matrix interface.

The additive manufacturing of Koch fibers and meshes with high complexity ratios in metallic materials is revealed to be a challenge at present, due to currently available technologies; the powder-bed EBM method used here for example, limits objects with fine features to a minimum size of close to ~0.4 mm (cf. Sections 3–5). Other processing technologies, for example those that use a laser, rather than an electron beam, as the heat source may allow better resolution, up to their own

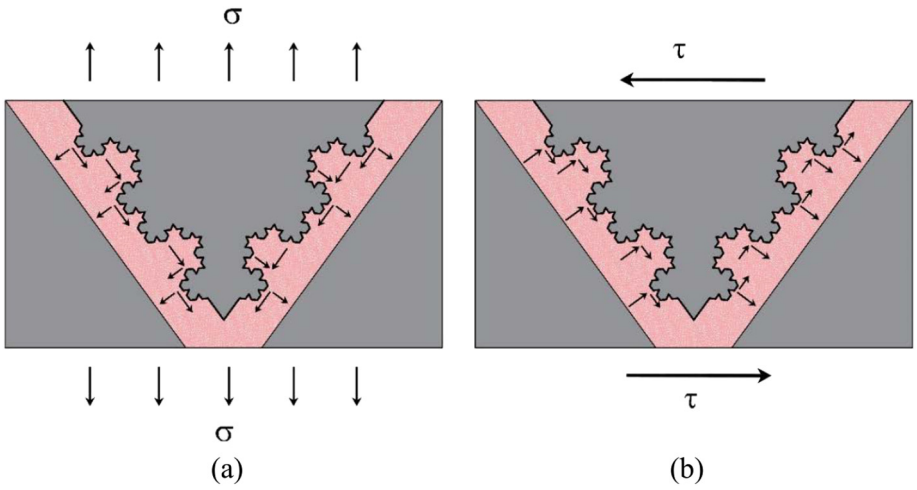

Fig. 13. Rigid tooth models of a Koch fiber – matrix interface loaded in tension (a) and compression (b) [25].

individual limits. It can be suggested that exploration of larger components at a scale above resolution limitations, including testing capabilities, may find favorable results and highlight the potential of fractal materials in structural composites. The physical and mechanical tests presented in Section 6 have however confirmed the great potential of metallic reinforcements with fractal architecture in terms of appreciable accuracy, when handling elements in the available range of precision (Section 6.1), and good mechanical properties of the AM processed parts (Section 6.3).

8. Concluding remarks

The proposed design strategy of reinforcing fibers and meshes with fractal architecture shows promise as an effective tool to create mortar and concrete composites that feature enhanced bond strength and energy dissipation capacity, due to fractal interlocking phenomena and the development of rough fracture surfaces at the fiber-matrix interface. Such effects can be achieved at a custom-designed scale, depending on the nature of the matrix material and loading conditions, through the fine tuning of the complexity parameters that govern the fractal design algorithm. The given results on the bending response of mortar specimens reinforced with Koch fibers have shown that such reinforcements are able to significantly enhance the first crack strength and the energy dissipation capacity of the material.

In closing, we point out a number of directions for future work that are needed to further explore the technological potential of fractal reinforcements for composite materials. First, scaling up of the component size may allow resolution issues to be minimised if powder-bed AM processes are to be used. Secondly, a variety of multiscale additive manufacturing technologies need to tested as viable tools for the AM of Koch fibers and meshes, one employing both metallic and polymeric materials. These may include Selective Laser Melting (SLM) using finer raw feedstock materials, and/or wire feed polymer technologies [59] or photopolymeric deposition sources among others. Such an endeavor to further advance the fabrication methods should be complemented by theoretical, numerical and experimental studies on the mechanical response of the matrix-reinforcement interface, which call for the adoption of multiscale mechanics approaches, advanced microscopy techniques, and high-resolution digital image correlation procedures [11–19].

Credit author statement

IF led the design of the fibers, contact angle tests and mechanical tests. EHN led the additive manufacturing of the fibers, the microstructure characterization and Vicker hardness tests. AdF led the 3d laser scanner surveys. FC supervised the design of the fibers, contact angle tests and mechanical tests. RG supervised the additive manufacturing of the fibers, the microstructure characterization and Vicker hardness tests. FF provided the subject and supervised all phases. All the authors contributed to discussion and concluding remarks, as well as to the writing and revision of the manuscript.

Acknowledgements

ADF and FF acknowledge financial support from the Italian Ministry of Education, University and Research (MIUR) under the 'Departments of Excellence' grant L.232/2016. RG would like to acknowledge a Fellowship supported by the Royal Academy of Engineering under the RAEng/Leverhulme Trust Senior Research Fellowships scheme. The authors wish to thank Prof. Salvatore Barba and Dr. Giuseppe Rocchetta from the Department of Civil Engineering of the University of Salerno for their collaboration with the laser scanning surveys and the mechnical tests presented in this manuscript, respectively.

Appendix A. Supplementary data

Supplementary data to this article can be found online at https://doi.org/10.1016/j.matdes.2019.107758.

References

[1] M.G. Rashed, M. Ashraf, R.A.W. Mines, P.J. Hazell, Metallic microlattice materials: a current state of the art on manufacturing, mechanical properties and applications, Mater. Des. 95 (2016) 518–533.
[2] I. Farina, F. Fabbrocino, G. Carpentieri, M. Modano, A. Amendola, R. Goodall, F. Fraternali, On the reinforcement of cement mortars through 3D printed polymeric and metallic fibers, Compos. Part B 90 (2016) 76–85.
[3] I. Farina, F. Fabbrocino, F. Colangelo, L. Feo, F. Fraternali, Surface roughness effects on the reinforcement of cement mortars through 3D printed metallic fibers. 2016, Compos. Part B 99 (2016) 305–311.
[4] I. Farina, M. Modano, G. Zuccaro, R. Goodall, F. Colangelo, Improving flexural strength and toughness of geopolymer mortars through additively manufactured metallic rebars, Compos. Part B 145 (2018) 155–161.
[5] H. Yue, V. Reguero, E. Senokos, A. Monreal-Bernal, B. Mas, J.P. Fernández-Blázquez, J.J. Vilatela, Fractal carbon nanotube fibers with mesoporous crystalline structure, Carbon 122 (2017) 47–53.
[6] F. De Nicola, P. Castrucci, M. Scarselli, F. Nanni, I. Cacciotti, M. De Crescenzi, Multifractal hierarchy of single-walled carbon nanotube hydrophobic coatings, Sci. Rep. 5 (2015) 8583.
[7] M. Yan, X. Tian, G. Peng, Y. Cao, D. Li, Hierarchically porous materials prepared by selective laser sintering, Mater. Des. 135 (2017) 62–68.
[8] S. Wang, B.Y. Guan, L. Yu, X.W. Lou, Rational design of three-layered TiO2@ carbon@ MoS2 hierarchical nanotubes for enhanced lithium storage, Adv. Mater. 29 (37) (2017) 1702724.
[9] V.A. Yolshina, L.A. Yolshina, V.A. Elterman, E.G. Vovkotrub, A.A. Shatunova, V.I. Pryakhina, N.V. Tarakina, Synthesis of and characterization of freestanding, high-

hierarchically structured graphene-nanodiamond films, Mater. Des. 135 (2017) 343–352.
[10] J. Dong, G. Zhang, X. Wang, S. Zhang, C. Deng, Cross-linked Na2VTi (PO4)3@C hierarchical nanofibers as high-performance bi-functional electrodes for symmetric aqueous rechargeable sodium batteries, J. Mater. Chem. A 5 (35) (2017) 18725–18736.
[11] J. Li, Z. Wu, C. Huang, L. Li, Multiscale carbon nanotube-woven glass fiber reinforced cyanate ester/epoxy composites for enhanced mechanical and thermal properties, Compos. Sci. Technol. 104 (2014) 81–88.
[12] H. Mei, Q. Bai, T. Ji, H. Li, L. Cheng, Effect of carbon nanotubes electrophoretically-deposited on reinforcing carbon fibers on the strength and toughness of C/SiC composites, Compos. Sci. Technol. 103 (2014) 94–99.
[13] Y. Jia, Z. Chen, W. Yan, A numerical study on carbon nanotube pullout to understand its bridging effect in carbon nanotube reinforced composites, Compos. Part B 81 (2015) 64–71.
[14] L. Feng, K. Li, B. Xue, Q. Fu, L. Zhang, Optimizing matrix and fiber/matrix interface to achieve combination of strength, ductility and toughness in carbon nanotube-reinforced carbon/carbon composites, Mater. Des. 113 (2017) 9–16.
[15] B.E.B. Uribe, E.M.S. Chiromito, A.J.F. Carvalho, R. Arenal, J.R. Tarpani, TEMPO-oxidized cellulose nanofibers as interfacial strengthener in continuous-fiber reinforced polymer composites, Mater. Des. 133 (2017) 340–348.
[16] X. Zheng, et al., Ultralight, ultrastiff mechanical metamaterials, Science 344 (2014) 6190.
[17] M.W. Moon, A. Vaziri, Surface modification using a multi-step plasma treatment, J. Scripta Mater. 60 (2009) 44–47.
[18] Q. Wu, R. Zhao, Q. Liu, T. Jiao, J. Zhu, F. Wang, Simultaneous improvement of interfacial strength and toughness between carbon fiber and epoxy by introducing amino functionalized ZrO2 on fiber surface, Mater. Des. 149 (2018) 15–24.
[19] C. Wang, X. Ji, A. Roy, V.V. Silberschmidt, Z. Chen, Shear strength and fracture toughness of carbon fibre/epoxy interface: effect of surface treatment, Mater. Des. 85 (2015) 800–807.
[20] B. Mandelbrot, The Fractal Geometry of Nature, W.H. Freeman, New York, 1982.
[21] Riddle, L.H. Koch Curve, http://ecademy.agnesscott.edu/~lriddle/ifs/kcurve/kcurve.htm (accessed 15 March 2019).
[22] Riddle, L.H. Koch Snowflake, http://ecademy.agnesscott.edu/~lriddle/ifs/ksnow/ksnow.htm (accessed 15 March 2019).
[23] Wolfram MathWorld, Koch snowflake, http://mathworld.wolfram.com/KochSnowflake.html (accessed 15 March 2019).
[24] M.M. Khoshhesab, Y. Li, Mechanical behavior of 3D printed biomimetic koch fractal contact and interlocking, Extreme Mechanics Letters 24 (2018) 58–65.
[25] Y. Li, C. Ortiz, M.C. Boyce, A generalized mechanical model for suture inter-faces of arbitrary geometry, Journal of the Mechanics and Physics of Solids 61 (4) (2013) 1144–1167.
[26] L. Djumas, A. Molotnikov, G.P. Simon, Y. Estrin, Enhanced mechanical performance of bio-inspired hybrid structures utilising topological interlocking geometry, Sci. Rep. 6 (2016), 26706.
[27] Gabriele, P.D., Robertson, J.H., Haggard, J.S., 2011. Tissue fiber scaffold and method for making, US Patent Application Publication, Publication No.: 2011/0076771 A1, https://patents.google.com/patent/US20110076771?oq=US2011%2f0076771 (accessed 15 March 2019).
[28] M. Mohsenizadeh, F. Gasbarri, M. Munther, A. Beheshti, K. Davami, Additively-manufactured lightweight metamaterials for energy absorption, Mater. Des. 139 (2018) 521–530.
[29] D.W. Abueidda, M. Bakir, R.K.A. Al-Rub, J.S. Bergström, N.A. Sobh, I. Jasiuk, Mechanical properties of 3D printed polymeric cellular materials with triply periodic minimal surface architectures, Mater. Des. 122 (2017) 255–267.
[30] E. Hernández-Nava, C.J. Smith, F. Derguti, S. Tammas-Williams, F. Léonard, P.J. Withers, I. Todd, R. Goodall, The effect of density and feature size on mechanical properties of isostructural metallic foams produced by additive manufacturing, Acta Mater. 85 (2015) 387–395.
[31] E. Hernández-Nava, S. Tammas-Williams, C. Smith, F. Leonard, P.J. Withers, I. Todd, R. Goodall, X-ray tomography characterisation of lattice structures processed by selective electron beam melting, Metals (Basel) 7 (8) (2017).
[32] V. Mechtcherine, J. Grafe, V.N. Nerella, E. Spaniol, M. Hertel, U. Füssel, 3D-printed steel reinforcement for digital concrete construction – manufacture, mechanical properties and bond behaviour, Constr. Build. Mater. 179 (2018) 125–137.
[33] MX3D Bridge, https://mx3d.com/projects/bridge-2/ (accessed 15 March 2019).
[34] S.S. Al-Bermani, M.L. Blackmore, W. Zhang, I. Todd, The origin of microstructural diversity, texture, and mechanical properties in electron beam melted Ti-6Al-4V, Metallurgical Transactions A, Physical Metallurgy and Materials Science 41 (13) (2010) 3422–3434.
[35] A.A. Antonysamy, J. Meyer, P.B. Prangnell, Effect of build geometry on the β-grain structure and texture in additive manufacture of Ti6Al4V by selective electron beam melting, Mater. Charact. 84 (2013) 153–168.
[36] P.A. Kobryn, S.L. Semiatin, The laser additive manufacture of Ti-6Al-4V, Journal of the Minerals, Metals & Materials Society 53 (9) (2001) 40–42.
[37] S.L. Semiatin, T.R. Bieler, The effect of alpha platelet thickness on plastic flow during hot working of Ti-6Al-4V with a transformed microstructure, Acta Materalia 49 (17) (2001) 3565–3573.
[38] D. Tabor, The Hardness of Metals, Claredon Press, Oxford, 1951.
[39] G. Lütjering, J.C. Williams, Titanium, Springer, Berlin, 2003.
[40] Z.J. Wally, A.M. Haque, A. Feteira, F. Claeyssens, R. Goodall, G.C. Reilly, Selective laser melting processed Ti6Al4V lattices with graded porosities for dental applications, J. Mech. Behav. Biomed. Mater. 90 (2019) 20–29.
[41] S. Rusinkiewicz and M. Levoy, "Efficient variants of the ICP algorithm," *Proceedings Third International Conference on 3-D Digital Imaging and Modeling*, Quebec City, Quebec, Canada, 2001, pp. 145–152.
[42] Konic Minolta, 3D Measurement, https://www.konicaminolta.com/instruments/ (accessed 15 March 2019).
[43] 3D Geomagic Studio Systems, https://it.3dsystems.com/press-releases/3d-systems-announces-geomagic-2014-1 2014, Accessed date: 15 March 2019.
[44] D.Y. Kwok, A.W. Neumann, Contact angle measurement and contact angle interpretation, Adv. Colloid Interf. Sci. 81 (3) (1999) 167–249.
[45] K. Law, H. Zhao, Surface Wetting: Characterization, Contact Angle, and Fundamentals. Surface Wetting: Characterization, Contact Angle, and Fundamentals, 2015 1–162.
[46] Y. Yuan, T.R. Lee, Contact angle and wetting properties, in: G. Bracco, B. Holst (Eds.), Surface Science Techniques. Springer Series in Surface Sciences, vol. 51, Springer, Berlin, Heidelberg, 2013.
[47] DataPhysics Instruments, OCA – Optical contact angle measuring and contour analysis systems. https://www.dataphysics-instruments.com/products/oca/ (accessed 15 March 2019).
[48] EN 1015-11 (2007). Methods of test for mortar for masonry – Part 11: determination of flexural and compressive strength of hardened mortar.
[49] S. Spadea, I. Farina, A. Carrafiello, F. Fraternali, Recycled nylon fibers as cement mortar reinforcement, Constr. Build. Mater. 80 (2005) 200–209.
[50] F. Colangelo, R. Cioffi, Use of cement kiln dust, blast furnace slag and marble sludge in the manufacture of sustainable artificial aggregates by means of cold bonding palletization, Materials 6 (8) (2016) 3139–3159.
[51] A. N. Hashim, A.N., et al. (2015). Characteristics of mortars with various composition of ground granulated blast furnace slag, Appl. Mech. Mater., 754-755, 305–309.
[52] Mobili, A., Belli, A., Giosuè, C., T. Bellezze, T., Tittarelli, F., (2016). Metakaolin and fly ash alkali-activated mortars compared with cementitious mortars at the same strength class, Cem. Concr. Res., 88, 198–210.
[53] M.S. Lorrain, L.F. Caetano, B.V. Silva, L.E.S. Gomes, M.P. Barbosa, L.C.P. Silva Filho, Bond strength and rib geometry: a comparative study of the influence of deformation patterns on anchorage bond strength, Proceedings of the 3rd International Fib Congress and Exhibition, Incorporating the PCI Annual Convention and Bridge Conference: Think Globally, Build Locally, D.C., USA, Washington, 2010.
[54] G. Metelli, G.A. Plizzari, Influence of the relative rib area on bond behaviour, Mag. Concr. Res. 66 (6) (2014) 277–294.
[55] D. Mezhoud, Y. Bouafia, M. Saad, J. Saliba, Bond-slip law and short tie behavior without main cracks, J. Adhes. Sci. Technol. 32 (14) (2018) 1578–1598.
[56] S. Islam, H.M. Afefy, K. Sennah, H. Azimi, Bond characteristics of straight- and headed-end, ribbed-surface, GFRP bars embedded in high-strength concrete, Constr. Build. Mater. 83 (2015) 283–298.
[57] J. Schlaich, K. Schaefer, Design and detailing of structural concrete using strut-and-tie models, Structural Engineer London 69 (6) (1991) 13p.
[58] R. Park, T. Paulay, Reinforced Concrete Structures, John Wiley & Sons, New York, 2001.
[59] R. Singh, S. Singh, F. Fraternali, Development of in-house composite wire based feed stock filaments of fused deposition modelling for wear-resistant materials and structures, Compos. Part B 98 (2016) 244–249.